Simulating binary neutron stars: Dynamics and gravitational waves

Matthew Anderson,[1] Eric W. Hirschmann,[2] Luis Lehner,[1] Steven L. Liebling,[3] Patrick M. Motl,[1] David Neilsen,[2] Carlos Palenzuela,[1] and Joel E. Tohline[1]

[1]*Department of Physics and Astronomy, Louisiana State University, Baton Rouge, Louisiana 70803-4001, USA*
[2]*Department of Physics and Astronomy, Brigham Young University, Provo, Utah 84602, USA*
[3]*Department of Physics, Long Island University–C.W. Post Campus, Brookville, New York 11548, USA*

(Received 20 August 2007; published 7 January 2008)

We model two mergers of orbiting binary neutron stars, the first forming a black hole and the second a differentially rotating neutron star. We extract gravitational waveforms in the wave zone. Comparisons to a post-Newtonian analysis allow us to compute the orbital kinematics, including trajectories and orbital eccentricities. We verify our code by evolving single stars and extracting radial perturbative modes, which compare very well to results from perturbation theory. The Einstein equations are solved in a first-order reduction of the generalized harmonic formulation, and the fluid equations are solved using a modified convex essentially non-oscillatory method. All calculations are done in three spatial dimensions without symmetry assumptions. We use the HAD computational infrastructure for distributed adaptive mesh refinement.

DOI: 10.1103/PhysRevD.77.024006 PACS numbers: 04.25.dk

I. INTRODUCTION

It is widely expected that gravitational waves of sufficiently strong amplitude will be detected by a new generation of gravitational wave interferometers. Binary systems composed of compact objects, such as black holes and/or neutron stars, are among the strongest expected sources of these waves. Advanced gravitational wave detectors should be sensitive enough to detect the merging phase of such binaries. A detailed analysis of the expected waveforms from these events will provide valuable information not only in the analysis of the received signals, but also in the design and tuning of future advanced gravitational wave detectors [1,2].

In relation to these efforts, and beyond the intrinsic importance of the two-body problem in general relativity (GR), it is significant that recent studies of the binary black hole problem have made substantial progress in providing waveforms for these mergers (see for instance [3–8]). Furthermore, these numerical results for vacuum spacetimes show a remarkable agreement with those obtained with approximation techniques [9,10]. This provides considerable support for the use of waveforms obtained via approximation techniques, suitably enhanced by further information from numerical simulations, since these can be more easily encoded in a template bank [11]. This requires knowing the waveforms during the premerger, merger, and postmerger stages and matching them appropriately to obtain the continuous wave train through the most violent and strongly radiative stage of the dynamics.

For nonvacuum spacetimes, differences in the waveforms may arise from the state of matter describing the compact stars, the influence of magnetic fields, and related phenomena. To fully understand these systems and their waveforms, detailed simulations will be required to map out the possible phenomenology.

For the particular case of binary neutron stars in full GR, several efforts studying the system in three dimensional settings have been presented in recent years [12–18]. However, the complexity and computational cost of these simulations has permitted investigators to consider only a portion of the interesting parameter space, and several of them have been restricted by symmetry considerations. Nevertheless, a number of interesting problems are beginning to be addressed, including the influence of stiff versus soft equations of state [18], a possible way to determine the innermost stable circular orbit [16], the dynamics of unequal-mass binaries [18], and even the possible existence of critical phenomena in the merging system [17].

Further exploration of these systems will require relaxing symmetry considerations, such as axisymmetry or equatorial symmetry, and expanding the space of initial configurations that can be successfully evolved. Moreover, the inclusion of additional physics such as magnetic fields will be important as these effects may play a major role in the resulting dynamics. For instance, the magnetorotational instability, which redistributes angular momentum in the system, can have a strong influence on the multipole structure of the central source and hence on the gravitational wave output of the system.

To date, work on black hole–neutron star binaries has been limited to a few cases [19–21]. As a result, our understanding of this type of system is still in its infancy. Needless to say, we have even more to understand about both types of compact binaries when their environments, which may include magnetic fields and radiation transport, are included. Indeed, both magnetic fields and radiation transport are expected to be key ingredients in modeling short, hard gamma-ray burst phenomena with compact binaries. Understanding such spectacular events requires the addition of these ingredients to the computational

 © 2008 The American Physical Society

infrastructure. The resulting numerical simulations should allow for new astrophysical insights.

The present work is intended as the first in a series of studies that examine the evolution of compact binary systems in full three dimensional general relativity. To this end, we have developed a general computational infrastructure, with solvers for the Einstein and relativistic magnetohydrodynamics (MHD) equations, that incorporates several novel features, which we discuss in the following sections. In Sec. II we describe our formulation of the equations for these systems. This includes expressing the Einstein equations in terms of a desirable symmetric hyperbolic property [22,23] and coupling them with the equations of relativistic MHD [24,25]. Section III presents our numerical implementation, such as integration techniques, distributed adaptive mesh refinement (AMR), and a tapered-grid algorithm that ensures stability and considerably reduces spurious reflections off artificial internal boundaries [26]. These ingredients let us simulate binary evolutions in which the stars begin with wider separations than has been done in earlier studies. We can extract gravitational radiation in the wave zone and place outer boundaries an order of magnitude beyond what has been done previously. As a result, contamination by boundary effects is negligible. Section IV presents a fairly stringent code test by considering the dynamics of a single Tolman-Oppenheimer-Volkoff (TOV) solution and extracting the radial oscillation modes of the star. Section V describes our main application, namely, a study of a binary neutron star system without any assumed symmetries. We follow the dynamics of the system from an early non-quasicircular stage to the merger and subsequent formation of a neutron star or a black hole. We present gravitational wave signals as measured by observers placed in the wave zone and calculated via Weyl scalars. Section VI concludes and offers some considerations for future work.

II. FORMULATION AND EQUATIONS OF MOTION

The binary neutron star systems considered here are governed by both the Einstein equations for the geometry and the relativistic fluid equations for the matter. We write both systems as first-order hyperbolic equations.

In this section we present a brief summary of our formulation and equations for both the geometry and the fluid. More details on our approach to the Einstein equations [22] and the relativistic fluid equations [24,25] can be found elsewhere. By way of notation, we use letters from the beginning of the alphabet (a, b, c) for spacetime indices, while letters from the middle of the alphabet (i, j, k) range over spatial components. We adopt geometric units where $c = G = 1$.

A. Einstein equations

We write the Einstein equations in a first-order reduction of the generalized harmonic (GH) formalism. Our approach is closely related to the one in [27], and it was used previously in binary boson star evolutions [22], where additional information can be found.

We define spacelike hypersurfaces at $x^0 \equiv t = \text{const}$, and define the 3-metric h_{ij} on the hypersurfaces. A vector normal to the hypersurfaces is given by $n_a = -\nabla_a t/||\nabla_a t||$, and coordinates defined on neighboring hypersurfaces can be related through the lapse, α, and shift, β^i. With these definitions, the spacetime metric g_{ab} can then be written as

$$\mathrm{d}s^2 = g_{ab}\mathrm{d}x^a\mathrm{d}x^b \tag{1}$$

$$= -\alpha^2\mathrm{d}t^2 + h_{ij}(\mathrm{d}x^i + \beta^i\mathrm{d}t)(\mathrm{d}x^j + \beta^j\mathrm{d}t). \tag{2}$$

Indices on spacetime quantities are raised and lowered with the 4-metric g_{ab} and its inverse, while the 3-metric h_{ij} and its inverse are used to raise and lower indices on spatial quantities.

In the generalized harmonic formulation, the evolved variables are

$$g_{ab}, \qquad Q_{ab} \equiv -n^c\partial_c g_{ab}, \qquad D_{iab} \equiv \partial_i g_{ab}, \tag{3}$$

namely, the spacetime metric and its temporal and spatial derivatives, respectively. Coordinates are specified via the generalized harmonic condition

$$\Box x^a = H^a(t, x^i), \tag{4}$$

where the arbitrary source functions $H^a(t, x^i)$ determine the coordinate freedom. Although our code allows for a general coordinate choice, we choose harmonic coordinates for the work presented here and set $H^a(t, x^i) = 0$.

The evolution equations in our GH formalism are

$$\partial_t g_{ab} = \beta^k D_{kab} - \alpha Q_{ab}, \tag{5}$$

$$\begin{aligned}\partial_t Q_{ab} = {} & \beta^k\partial_k Q_{ab} - \alpha h^{ij}\partial_i D_{jab} - \alpha\partial_a H_b - \alpha\partial_b H_a \\ & + 2\alpha\Gamma_{cab}H^c + 2\alpha g^{cd}(h^{ij}D_{ica}D_{jdb} - Q_{ca}Q_{db} \\ & - g^{ef}\Gamma_{ace}\Gamma_{bdf}) - \frac{\alpha}{2}n^c n^d Q_{cd}Q_{ab} \\ & - \alpha h^{ij}D_{iab}Q_{jc}n^c - 8\pi\alpha(2T_{ab} - g_{ab}T) \\ & - 2\sigma_0\alpha[n_a Z_b + n_b Z_a - g_{ab}n^c Z_c] \\ & + \sigma_1\beta^i(D_{iab} - \partial_i g_{ab}),\end{aligned} \tag{6}$$

$$\begin{aligned}\partial_t D_{iab} = {} & \beta^k\partial_k D_{iab} - \alpha\partial_i Q_{ab} + \frac{\alpha}{2}n^c n^d D_{icd}Q_{ab} \\ & + \alpha h^{jk}n^c D_{ijc}D_{kab} - \sigma_1\alpha(D_{iab} - \partial_i g_{ab}).\end{aligned} \tag{7}$$

Here T_{ab} is the stress-energy tensor and T is its trace, $T = T^a{}_a$. Z^a is a vector related to the constraints defined below in Eq. (11). These variables are not evolved; rather, they measure the constraint violation and are included in the evolution equations for constraint damping purposes [28]. We also define $\Gamma_{abc} = g_{ad}\Gamma^d{}_{bc}$, where $\Gamma^a{}_{bc}$ are the

Christoffel symbols obtained from g_{ab}, given by

$$\Gamma^a{}_{bc} = \tfrac{1}{2} g^{ad}(D_{bdc} + D_{cdb} - D_{dbc}). \tag{8}$$

Note that D_{iab} are evolved variables in our system, and the quantities D_{0ab} are computed from Q_{ab} and D_{iab} via

$$D_{0ab} = -\alpha Q_{ab} + \beta^k D_{kab}. \tag{9}$$

While the Arnowitt-Deser-Misner (ADM) extrinsic curvature is not part of the GH system, the fluid equations below are written in terms of K_{ij}, which can be calculated as

$$K_{ij} = \frac{1}{2} Q_{ij} + \frac{1}{\alpha}(D_{(ij)0} - \beta^k D_{(ij)k}). \tag{10}$$

This GH formulation includes a number of constraints that must be satisfied for consistency, including the Hamiltonian and momentum constraints as well as additional constraints that arise in the first-order reduction. In particular, if we define the four-vector

$$2Z^a \equiv -\Gamma^a{}_{bc} g^{bc} - H^a(t, x^i), \tag{11}$$

it can be shown that the energy and momentum constraints are satisfied if $Z^a = 0 = \partial_t Z^a$. The free parameters σ_0 and σ_1 are chosen to control the damping of the four-vector Z_a (the energy and momentum constraints) and the first-order constraints, respectively [22,27]. We monitor the Z^a during the evolution as an indication of the magnitude of the numerical error in the solution.

B. Perfect fluid equations

We now briefly introduce the perfect fluid equations. Additional information can be found in our previous work [24,25] as well as in general review articles [29,30].

The stress-energy tensor for the perfect fluid is

$$T_{ab} = h_e u_a u_b + P g_{ab}, \tag{12}$$

where u^a is the four-velocity of the fluid, h_e is the enthalpy, and P is the isotropic pressure. The enthalpy can be written

$$h_e = \rho_o + \rho_o \epsilon + P, \tag{13}$$

where ρ_o is the rest energy density and ϵ is the specific internal energy density. We introduce the quantities

$$W \equiv -n^a u_a, \qquad v^i \equiv \frac{1}{W} h^i_j u^j, \tag{14}$$

where W is the Lorentz factor between the fluid frame and the fiducial ADM observers and v^i is the spatial coordinate velocity of the fluid. The set of fluid variables introduced here are known as the *primitive* variables, $\boldsymbol{w} = (\rho_o, v^i, P)^{\mathrm{T}}$.

High resolution shock capturing schemes (HRSC) are robust numerical methods for compressible fluid dynamics. These methods, based on Godunov's seminal work [31], are fundamentally based on writing the fluid equations as integral conservation laws. To this end, we introduce *conservative* variables $\boldsymbol{q} = (D, S_i, \tau)^{\mathrm{T}}$, where

$$D = W\rho_o, \tag{15}$$

$$S_i = h_e W^2 v_i, \tag{16}$$

$$\tau = h_e W^2 - P - D. \tag{17}$$

In an asymptotically flat spacetime these quantities are conserved, and are related to the baryon number, momentum, and, in the nonrelativistic limit, the kinetic energy, respectively. Anticipating the form of the evolution equations, we also introduce the densitized conserved variables

$$\tilde{D} = \sqrt{h} D, \qquad \tilde{S}_i = \sqrt{h} S_i, \qquad \tilde{\tau} = \sqrt{h}\tau, \tag{18}$$

where $h = \det(h_{ij})$. The fluid equations can now be written in balance law form,

$$\partial_t \tilde{\boldsymbol{q}} + \partial_k \boldsymbol{f}^k(\tilde{\boldsymbol{q}}) = \boldsymbol{s}(\tilde{\boldsymbol{q}}), \tag{19}$$

where $\boldsymbol{f}^k$ are flux functions and $\boldsymbol{s}$ are source terms. The fluid equations in this form are specifically

$$\partial_t \tilde{D} + \partial_i\left[\alpha \tilde{D}\left(v^i - \frac{\beta^i}{\alpha}\right)\right] = 0, \tag{20}$$

$$\partial_t \tilde{S}_j + \partial_i\left[\alpha\left(\tilde{S}_j\left(v^i - \frac{\beta^i}{\alpha}\right) + \sqrt{h} P h^i{}_j\right)\right] = \alpha^3 \Gamma^i{}_{jk}(\tilde{S}_i v^k + \sqrt{h} P h_i{}^k) + \tilde{S}_a \partial_j \beta^a - \partial_j \alpha(\tilde{\tau} + \tilde{D}), \tag{21}$$

$$\partial_t \tilde{\tau} + \partial_i\left[\alpha\left(\tilde{S}^i - \frac{\beta^i}{\alpha}\tilde{\tau} - v^i \tilde{D}\right)\right] = \alpha\left[K_{ij}\tilde{S}^i v^j + \sqrt{h} K P - \frac{1}{\alpha}\tilde{S}^a \partial_a \alpha\right]. \tag{22}$$

Here ${}^3\Gamma^i{}_{jk}$ is the Christoffel symbol associated with the 3-metric h_{ij}, and K is the trace of the extrinsic curvature, $K = K^i{}_i$.

Finally, we close the system of fluid equations with an equation of state (EOS). We choose the ideal gas EOS

$$P = (\Gamma - 1)\rho_o \epsilon, \tag{23}$$

where Γ is the constant adiabatic exponent. Nuclear matter in neutron stars is relatively stiff, and we set $\Gamma = 2$ in this work. When the fluid flow is adiabatic, this EOS reduces to the well-known polytropic EOS

$$P = \kappa \rho_o{}^{\Gamma}, \tag{24}$$

where κ is a dimensional constant. We use the polytropic EOS only for setting initial data.

III. NUMERICAL APPROACH

Our numerical approach to solving the combined equations of general relativistic hydrodynamics (GRHD) is built upon two extensively tested codes: These were written to solve (1) the Einstein equations [22,23] and (2) the

relativistic MHD equations [24,25]. It should be mentioned that, while we do solve the full GRMHD equations, in our current work the magnetic field is set to zero. Results with nontrivial magnetic fields will be presented elsewhere [32].

While both sets of evolution equations are hyperbolic, the solutions from each set of equations are quite different. The Einstein equations are linearly degenerate, and therefore we expect smooth solutions to evolve from smooth initial data. The fluid equations, on the other hand, are genuinely nonlinear, and discontinuous weak solutions (shocks) generically evolve from smooth initial data [33]. We choose numerical methods adapted to the features of each set of equations. The fluid equations are evolved with a modified convex essentially non-oscillatory (CENO) method, while the Einstein equations are evolved using fourth-order accurate difference operators that satisfy summation by parts (SBP). These very different methods are easily combined by discretizing the equations in time using the method of lines.

We base our code on the HAD computational infrastructure for distributed AMR. The Einstein and fluid solvers are written in separate modules, which can be used individually or combined. The following sections review our methods.

A. Adaptive mesh refinement using HAD

The neutron star problem has several important physical scales, and each must be adequately resolved to capture the relevant dynamics. These scales include (1) the individual stars, preferably incorporating some of their internal dynamics, (2) the orbital length scale, (3) the gravitational wave zone, and (4) the location of outer boundaries. In this work, the initial orbital scale is on the order of several stellar radii, the gravitational waves are extracted at 30, 40, and 50 stellar radii, and the outer boundaries of the computational domain are placed about 100 stellar radii from the orbital pair to reduce boundary contamination of the orbital dynamics and gravitational wave signals. The computational demands required to resolve these different physical scales are best met using adaptive mesh refinement.

We use the publicly available computational infrastructure HAD to provide parallel distributed AMR for our codes [34,35]. HAD can solve both hyperbolic and elliptic equations, and, unlike several other publicly available AMR toolkits [36–40], it accommodates both vertex and cell centered algorithms. HAD has a modular design, allowing one to solve different sets of equations with the same computational infrastructure. Furthermore, solvers for different equations can be coupled together, as we have done here with separate solvers for the GR and MHD equations. HAD provides Berger-Oliger [41] style AMR with subcycling in both space and time. The HAD clustering algorithm is Berger-Rigoutsos [42], and the load balancing algorithm is the least loaded scheme [43]. Refinement in HAD can be triggered by user-specified criteria, e.g., refining on solution features such as gradients or extrema, or refining on truncation error estimation using a shadow hierarchy. The runs presented here use the shadow hierarchy for refinement, and all dynamic fields are used to estimate the truncation error. Some additional fixed refinement regions are used for gravitational wave extraction in the wave zone. As an example, Fig. 1 illustrates the resulting mesh structure at a premerge stage in our simulations.

HAD supports arbitrary orders of accuracy [26], and the overall accuracy for the implementation employed here is third order for smooth solutions. HAD implements the tapered-grid boundary method for internal boundaries [26]. This method is advantageous for two reasons. It guarantees stability of the AMR algorithm if the unigrid counterpart is stable and also significantly reduces spurious reflections at interface boundaries.

Finally, when a fine grid is created during an evolution, the geometric variables are interpolated onto the fine grid using Lagrangian interpolation. The fluid variables are interpolated using weighted essentially non-oscillatory (WENO) interpolation [44]. This interpolation scheme is designed for discontinuous functions and reduces to Lagrangian interpolation for smooth functions.

B. Method of lines

The numerical methods for the Einstein equations (SBP) and the fluid equations (CENO) both specify the discretization of the spatial difference operators, giving the semi-discrete equations

$$\frac{d\boldsymbol{u}}{dt} = L(\boldsymbol{u}). \tag{25}$$

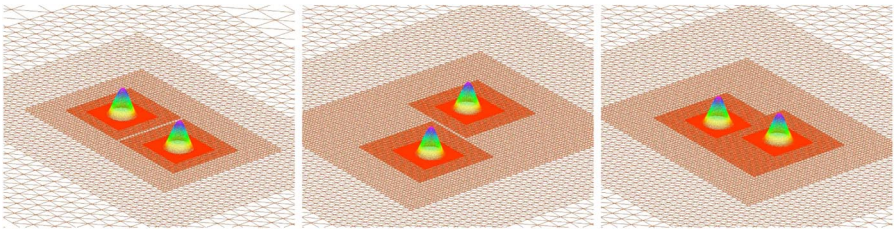

FIG. 1 (color online). The AMR mesh structure at times 0, 84, and 500 for the premerge stage of the simulation with resolution of 32 points across each star. The simulation had seven levels of refinement, five of which are visible here. Simulations were performed on 128 processors.

Here $\boldsymbol{u}$ represents the set of all variables evolved in both the Einstein and fluid equations, and L represents a discrete spatial difference operator. These ordinary differential equations are now discretized in time using the method of lines. We choose a third-order Runge-Kutta scheme that preserves the TVD (total variation diminishing) condition [45] to integrate the semidiscrete equations

$$\begin{aligned} \boldsymbol{u}^{(1)} &= \boldsymbol{u}^n + \triangle t L(\boldsymbol{u}^n), \\ \boldsymbol{u}^{(2)} &= \tfrac{3}{4}\boldsymbol{u}^n + \tfrac{1}{4}\boldsymbol{u}^{(1)} + \tfrac{1}{4}\triangle t L(\boldsymbol{u}^{(1)}), \\ \boldsymbol{u}^{(n+1)} &= \tfrac{1}{3}\boldsymbol{u}^n + \tfrac{2}{3}\boldsymbol{u}^{(2)} + \tfrac{2}{3}\triangle t L(\boldsymbol{u}^{(2)}). \end{aligned} \tag{26}$$

Using the method of lines for the temporal discretization gives us considerable freedom in choosing numerical methods for the spatial derivatives, as well as the ability to choose methods of arbitrary orders of accuracy. This freedom allows us to naturally and consistently combine both the CENO and SBP methods in the GRHD code.

C. Einstein equations

As described in [22] our implementation of the Einstein equations takes advantage of several techniques tailored to the symmetric hyperbolic properties of the generalized harmonic formulation we use. At the linear level, these techniques guarantee that the full AMR implementation is stable. We use second and fourth-order spatial derivative operators which satisfy summation by parts. These operators allow one to obtain a semidiscrete energy estimate which, together with suitable boundary conditions and time integration, ensures the stability of the implementation of linear systems (see [46], and also [47] and references cited therein). Relatedly, we employ a Kreiss-Oliger dissipation operator which is consistent with the summation by parts property.

For the outer boundaries, we implement Sommerfeld boundary conditions and follow the prescription given in [48]. We have also used maximally dissipative boundary conditions, but found that they led to larger reflections at the boundaries which, in turn, corrupt the waveform extraction at late times.

We set the constraint damping parameters to $\sigma_0 = \sigma_1 = 1$. These values were previously used in both binary black hole and boson star evolutions, and work similarly in the binary neutron star evolutions presented here. For the cases discussed here, constraint violations remain under control during the evolutions.

Finally, while our GH formalism allows for general coordinate choices through the source functions $H^a(t, x^i)$, we adopt $H^a(t, x^i) = 0$ in all the simulations described here. Thus, the coordinates adopted are strict harmonic coordinates.

D. Perfect fluid equations

The perfect fluid equations are integrated using a HRSC solver based on the CENO method [49], incorporating some modifications by Del Zanna and Bucciantini [50]. Detailed discussions of our method have been presented previously [24,25].

We choose the CENO method to solve the fluid equations primarily for two reasons. This means that the discrete fluid solution corresponds to point values of the solution and not cell averages. First, it is a finite difference or vertex centered scheme. As the Einstein equations are discretized with finite differences, coupling these equations to the fluid equations with AMR is simplified if both sets of variables are defined at the same grid locations. Second, CENO uses a componentwise decomposition (central schemes) of the equations rather than a spectral decomposition (upwind schemes). Central schemes are more efficient than spectral decomposition schemes. Although they are more diffusive at discontinuities, their solutions often differ only slightly from those obtained using upwind methods. With AMR we can sharply resolve all interesting features of the solution. Outflow boundary conditions are applied at the physical outer boundary.

The HLLE flux is used for the numerical flux [51]. This is a central-upwind method that uses the largest eigenvalues of the Jacobian matrix in each direction. To calculate the numerical fluxes, we choose to use piecewise parabolic method (PPM) reconstruction for the fluid variables [52], and reconstruct the primitive variables. No dissipation or discontinuity detection is used in the reconstruction. This is a bit of a departure from the CENO scheme. In general, ENO methods use a hierarchical reconstruction, where, for example, a second-order reconstruction depends on an underlying first-order reconstruction. We have found, at least for the resolutions considered here, that CENO often favors a first-order reconstruction at the center of stars, because of the manner in which candidate second-order stencils are compared for their similarity to the first-order reconstruction. This loss of accuracy at the center of the star damps the physical quasinormal oscillations of the star, and can lead to a long-term growth of the central density. PPM gives a superior reconstruction for stellar interiors, and therefore we adopt this reconstruction here. When the fluid flow is highly relativistic, the reconstruction procedure can produce unphysical states. When this occurs, we attempt reconstruction using a lower order. For example, if PPM fails, then a linear minmod reconstruction is attempted, and if this fails, then no reconstruction is used.

A consequence of using HRSC methods is the need to go back and forth between primitive, $\boldsymbol{w}$, and conservative, $\boldsymbol{q}$, variables. While the relation of the conservative variables in terms of the primitive variables is algebraic, the transformation that gives the primitive variables in terms of the conservative variables is transcendental. We use a Newton-

Raphson solver designed for the MHD equations to find the primitive variables [24]. At grid points where this solver may fail, the primitive variables are obtained from neighboring points by linear interpolation. The conservative variables are then recalculated at these points from the interpolated primitive variables.

Unphysical states can arise during the evolution of the fluid equations. This often occurs in evacuated regions of the grid, where truncation errors or effects from finite precision arithmetic are significant compared to the fluid densities. To compensate for some of these errors, a floor is applied to the energy variables $\tilde{D}$ and $\tilde{\tau}$ as

$$\tilde{D} \leftarrow \max(\tilde{D}, \text{floor}), \tag{27}$$

$$\tilde{\tau} \leftarrow \max(\tilde{\tau}, \text{floor}). \tag{28}$$

The floor in these runs is set between 1×10^{-8} and 5×10^{-9}, which is 7 orders of magnitude smaller than the central rest mass densities (ρ_c) of the individual stars. The floor value must be small compared to the densities in the problem so that the floor does not significantly affect the dynamics of interest. Often the effect of the floor can only be ascertained by varying it in a series of runs. For example, we found that floor values of 10^{-7} are too large, producing a noticeable increase in ρ_c during the evolutions, and changes in the stellar trajectories and the emitted waveforms. These errors essentially disappear when the floor is 10^{-8}, and reducing it further to 5×10^{-9} does not change the solutions. Thus, we adopt here a floor of 1×10^{-8}.

IV. OSCILLATING MODES OF SINGLE TOV STARS

As a first test of our combined GRHD code we consider a single TOV star. Our goal is not only to represent the analytic TOV solution, but to accurately reproduce the known radial oscillation modes of the star. While the TOV solution is spherically symmetric and static, discretization effects act as small perturbations that excite the normal modes of the star.

The initial data for this test consist of a $\Gamma = 2$ polytrope with $\kappa = 1$. (The solution is calculated using a modified version of the RNS code of Stergioulas [53].) The star, in the geometrized units with $\kappa = 1$, has a mass of $M = 0.14$, a circumferential radius $R = 0.958$, and central rest mass density $\rho_c = 1.28 \times 10^{-1}$. We evolve the data in a dynamic spacetime at different resolutions and using different reconstruction methods for the fluid variables. Figure 2 shows ρ_c plotted as a function of time for three resolutions of 32, 64, 128 points across the star. As expected, the oscillations and overall drift in ρ_c converge with resolution. This is important both as a code test and an indication of the resolution necessary to capture some dynamics of stellar interiors. The data in Fig. 2 were generated using PPM reconstruction. We found that first- and second-order CENO reconstructions were more diffusive, resulting in larger drifts in ρ_c. Consequently, we had difficulty in reproducing the radial pulsation modes of the star using these reconstructions.

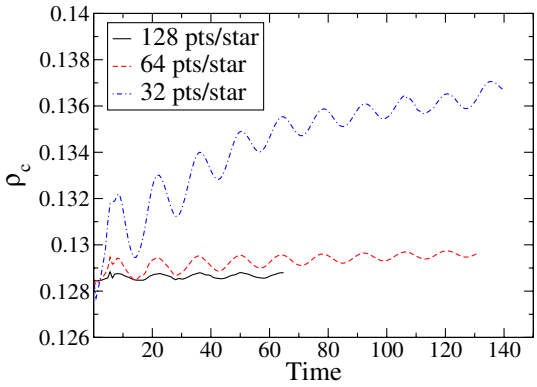

FIG. 2 (color online). This figure shows oscillations in the central rest energy density, ρ_c, for a dynamic spacetime evolution of a single TOV star at three different resolutions: 32, 64, and 128 points across the star. The initial data are for a star of mass $M = 0.14$, circumferential radius 0.958, central rest mass density $\rho_c = 1.28 \times 10^{-1}$, $\Gamma = 2$, and $\kappa = 1$. The outer boundary of the simulations is 12 stellar radii away from the center of the star, and PPM is used to reconstruct the fluid variables. While ρ_c increases noticeably for the coarsest resolution run, it eventually stabilizes at a higher value, giving a stable configuration. Results from the Fourier transform of this data are given in Table I. Owing to the computational costs of these simulations, the higher resolution runs were not evolved to the same end time. In particular, the highest resolution run was evolved only until $t \simeq 65$.

To confirm that the code reproduces the expected physical behavior, we examine the radial pulsations of the star. The modes are calculated from the oscillations in ρ_c, and the extracted frequencies are shown in Table I. (Though we present data for the central density only here, we have verified that these are global modes by examining the time variation of density and velocity in the star.) These oscillation modes can be compared to the known radial perturbation modes [54], and these frequencies are in excellent agreement. Note that to make these comparisons we

TABLE I. Comparison of small radial pulsation frequencies for an evolved star using the 3D GRHD code to the linear perturbation modes [54]. The polytrope is constructed for $\Gamma = 2$ and $\kappa = 1$. The perturbation results have been appropriately rescaled for $\kappa = 1$ [55]. The Fourier transform of the central density time series is plotted in Fig. 3.

Mode	3D GRHD code (kHz)	Perturbation results (kHz)	Relative difference (%)
F	14.01	14.42	2.88
H1	39.59	39.55	0.1
H2	59.89	59.16	1.2
H3	76.94	77.76	1.1

rescale the perturbation results as described in the Appendix, which were calculated for $\kappa = 100$. These validations are a stringent test of our computational methods and give us considerable confidence that our code accurately reproduces the physics of these systems.

V. BINARY NEUTRON STARS

In this paper, we consider two different binary neutron star mergers, one resulting in a prompt collapse to a black hole and one that results in a differentially rotating neutron star which persists for a long time (as compared to an orbital time close to merger). We evolve the systems through several orbits and extract gravitational radiation from the orbiting phase and the merger. In the course of performing these evolutions, we carefully examine some numerical questions to ensure the accuracy of our results.

Initial data for both binaries are set by superposing the initial data for single, boosted TOV stars [56]. Provided that the initial separation between stars is sufficiently large, violations in the momentum and Hamiltonian constraints are at or below the truncation error threshold. We monitor that this is indeed the case for our chosen separations by evaluating the constraints and checking that any violations are of the same order as those obtained for the single stars considered in the previous section. Thus, these data are numerically consistent. The boost velocities are smaller than the corresponding Keplerian velocities for Newtonian circular orbits. Thus, our data are not quasicircular (as used in [12,15]), and they do not correspond to a system resulting from a long, slow inspiral. However, these data allow us to both test our implementation and to examine how radiative effects circularize the orbits. Forthcoming work will consider initial data taken from post-Newtonian and quasiequilibrium approaches.

We extract the gravitational wave information by computing the Weyl scalar Ψ_4, and for convenience we further decompose $r\Psi_4$ as an expansion in terms of (spin-weighted) spherical harmonics,

$$r\Psi_4 = \sum_{l,m} C_{l,m}\,{}^{(-2)}Y_{lm}. \tag{29}$$

This extraction is done at three different locations from the center of mass, and we shift the obtained quantities in time to account for the travel time between the observers along null rays. These observers are placed within the wave zone, and the shift in time is given simply by the distance in Minkowski spacetime between the observers. As we consider here only equal-mass binaries, corrections for gauge effects should be small [57]. An analysis of these effects for different binaries will be presented elsewhere [58].

As discussed in [15], boundary and resolution effects can strongly influence the dynamics of these systems. To explore the effects of outer boundaries on the simulation results, we perform two otherwise identical evolutions with outer boundaries at different locations. While a more detailed discussion of these tests follows below in Sec. VA, we find that outer boundaries at 80 stellar radii have negligible influence on the solution. To examine resolution effects, we adopt a threshold error tolerance for the shadow hierarchy such that the resulting mesh covers each star with a minimum of 16 points. While in the previous section we used much higher resolutions to capture the interior dynamics of single stars, binary evolutions at similar resolutions here are prohibitively expensive. Figure 4 gives an indication of the minimum resolution required to evolve the binary without resolving the internal dynamics of individual stars. Figure 5 shows the (coordinate) radial distance between the center of the stars versus time for the three different resolutions. The trajectories converge as the resolution is increased.

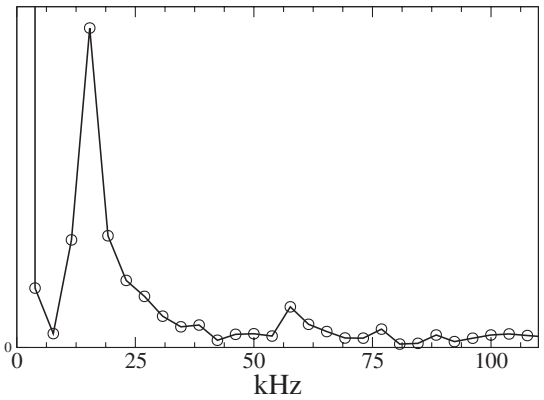

FIG. 3. This figure shows the Fourier transform of the oscillations of ρ_c seen in the highest resolution simulation of Fig. 2. Five distinct peaks are observed; the first four peaks are compared with results found via linear perturbation (see Table I). The scale of the vertical axis is arbitrary.

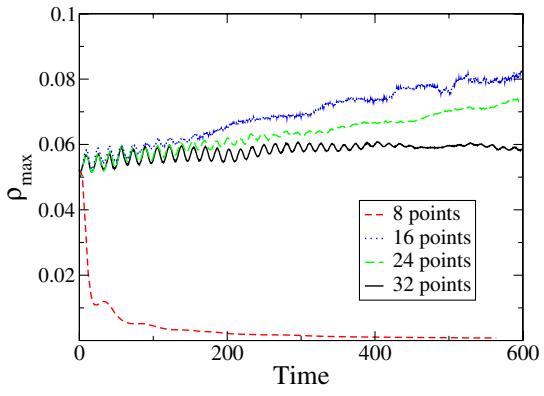

FIG. 4 (color online). This figure shows the maximum value of ρ_o in binary simulations at four resolutions: 8, 16, 24, and 32 points across each star. With fewer than 16 points across the star, the stars disperse. For increasing resolutions, the solutions converge.

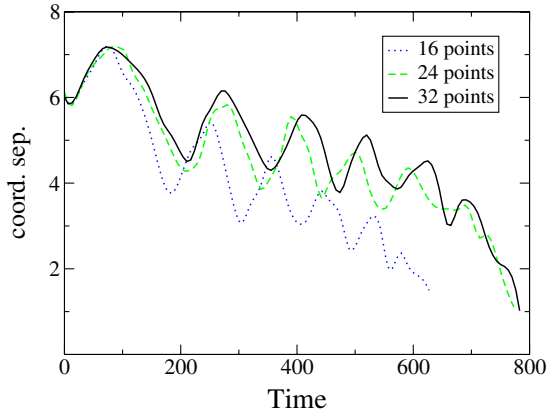

FIG. 5 (color online). The coordinate separation between the stars in a merging binary is shown here as a function of time for three resolutions. Notice that the merger time, about $t = 800$, is almost the same for the two finer resolutions.

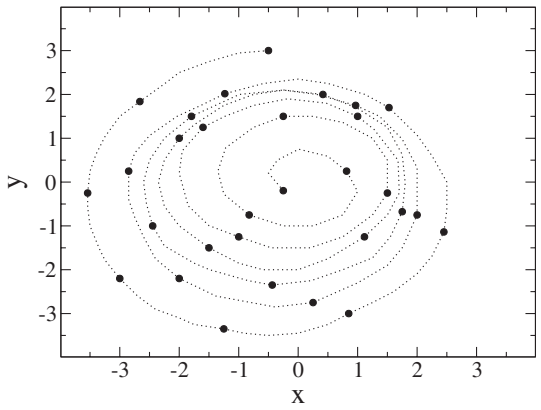

FIG. 7. The coordinate trajectory of the center of one of the neutron stars as it spirals into a black hole end state. The points (filled circles) that have been included along the trajectory are the coordinate locations of the maximum density. These points are shown at intervals of $\Delta t = 20$ in order to give an idea of the star's speed.

A. Black hole final state

The first set of initial data gives a binary neutron star merger that results in a prompt collapse to a black hole. As mentioned previously, the initial data are constructed from superposing two equal-mass neutron stars with zero spin angular momentum. In particular, each star has a mass of $M = 0.89\ M_\odot$, a radius of $R = 16.26$ km, and a central density of 3.24×10^{14} g/cm^3. The stars are placed initially at the coordinate locations $(x, y, z) = (0, \pm 3, 0)$ with the boost $v^i = (\mp 0.08, 0, 0)$.

We first investigate possible effects from the outer boundaries on the simulation results by performing two otherwise identical evolutions with the outer boundaries at different locations. In one, the outer boundary is at $80R$, and in the other it is at $124R$. These simulations use the shadow hierarchy, and the AMR grid structure is determined by the threshold error parameter. An additional set of fixed fine grids is placed at larger distances to ensure sufficient resolution for computing waveforms. As a consequence, the grid structure in the central region is determined dynamically while at far distances it is kept fixed. We compare the $C_{2,2}$ component of the gravitational wave signal measured by an observer at a fixed coordinate distance, $50R$, for the two computational domains. These waveforms are shown in Fig. 6, which shows only small differences in the waveforms at late times. Additional tests indicate that these differences arise from the location of the exterior, fixed refinement boxes. This observation is indicated by the coincidence of results obtained with outer boundaries at $100R$ and $80R$ with exactly the same coordinate locations of the exterior grids. The overall excellent agreement between the wave signals suggests that the influence of the boundary location is negligible.

The dynamics of the subsequent evolution shows a clear eccentricity which is reflected both in the gravitational waveforms (bottom panel of Fig. 6) and the coordinate trajectories (Fig. 7). It is worth noting that, following the

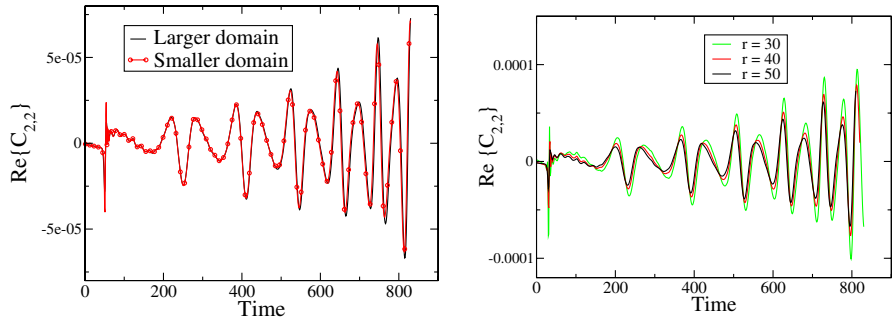

FIG. 6 (color online). Top panel: The $\ell = 2$, $m = 2$ mode of $r\Psi_4$ extracted at 50 stellar radii for binary simulations with different domain sizes. The smaller domain is of size ± 80 stellar radii while the larger is ± 124 stellar radii. The two results differ only by a small phase and amplitude error which appears late in the evolution. For both simulations, the floor value is 1×10^{-8}. Bottom panel: This includes three plots of the $\ell = 2$, $m = 2$ mode of $r\Psi_4$ extracted at 30, 40, and 50 stellar radii. The initial data are described in Sec. VA. The domain of the calculation is 248 stellar radii across. The signals from different extraction surfaces are shifted in time by the appropriate (flat-space) differences between the extraction radii.

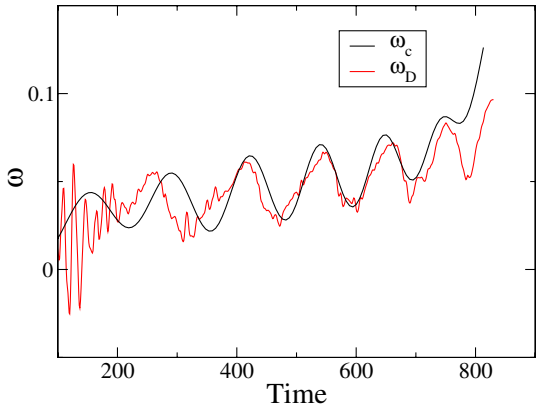

FIG. 8 (color online). Orbital frequency of the binary as calculated from the numerical evolution in two different ways. ω_c is obtained by following the coordinate position of the centers of the stars, while ω_D is obtained from the dominant mode of $r\Psi_4$.

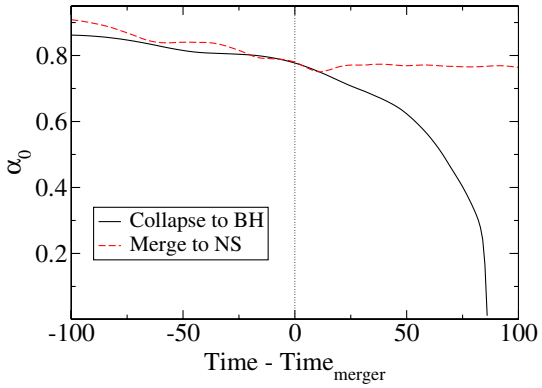

FIG. 10 (color online). The lapse at the origin as a function of time for the orbiting polytropes and their merger to either a black hole or neutron star. For the sake of comparison, we have defined $t_{\rm merger}$ to be the instant at which the stars come into contact. See Figs. 12 and 14 for contour plots of the lapse in the two cases.

suggestion of [9], a waveform similar to Fig. 6 can be obtained by using the Newtonian quadrupole approximation with the coordinate trajectories from Fig. 7. In addition, these trajectories are similar to those obtained by integrating the 2.5 post-Newtonian equations. Finally, as with the black hole case reported in [9], the orbital coordinate frequency ω_c (computed from the coordinate trajectories) is in good agreement with the orbital waveform frequency ω_D (computed from the dominant mode $\ell = 2$, $m = 2$ of $r\Psi_4$), as shown in Fig. 8.

The eccentricity can be computed using the Newtonian definition given in [59],

$$e = \frac{\sqrt{\omega_p} - \sqrt{\omega_a}}{\sqrt{\omega_p} + \sqrt{\omega_a}}, \tag{30}$$

where ω_p is the orbital frequency at a local maximum and ω_a the subsequent local minimum. The eccentricity of this simulation is shown in Fig. 9. To compute this, we take

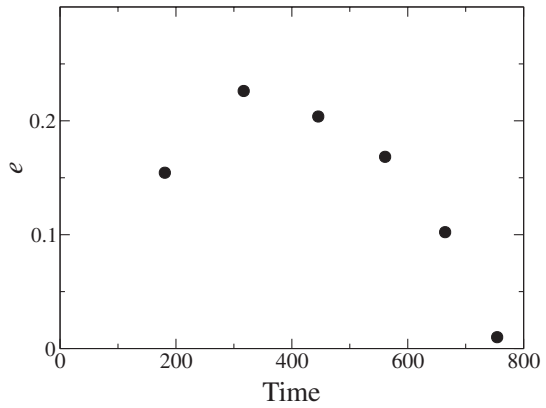

FIG. 9. The eccentricity obtained from Eq. (30). After a transient behavior due to the initial configuration, an overall monotonically decreasing behavior is seen in the eccentricity as the binary orbit becomes tighter.

each half-cycle and evaluate expression (30), thus obtaining a discrete set of values. The first point is clearly affected by the initial data adopted, but the subsequent points show an overall decrease towards zero. This is expected as the gravitational radiation carries away angular momentum, and its loss circularizes the orbit.

Upon merger, the object's pressure and rotation cannot support the star and it quickly collapses to a black hole. As described earlier, our simulations are carried out with harmonic slicing which is not singularity avoiding [60]. Although the lapse collapses to zero as illustrated in Fig. 12, it does not collapse sufficiently fast to avoid numerical problems. As a result, the size of the merged object decreases rapidly and the code crashes when it can no longer resolve the physical length scales within the allowed maximum refinement levels as shown in the final frame of Fig. 11. Ongoing work excises a region within a trapped surface to avoid this problem. We defer to future work a full analysis of the postmerger case and the transition to a quasinormal ringing pattern in the radiation [61].

B. Differentially rotating neutron star

In the case where the individual stars are initially separated (in coordinate space) by $4R$ and boosted with a speed of 0.0825, the merger does not give rise to a prompt collapse to a black hole; rather, it produces a single differentially rotating star. (See Figs.13 and 14.) As in the previous case, the initial orbital dynamics correspond to an eccentric inspiral trajectory. But upon merger, the object's pressure and rotation are sufficient to support a newly formed star. The merged object has a barlike structure that is spinning with a characteristic pattern frequency. The real part of the coefficient $C_{2,2}$ of $r\Psi_4$ for this evolution (shown here in Fig. 15) carries a signature of the merger (t approximately from 100 to 200) and of the resulting spinning bar (t greater than 250). Qualitatively, the outcome of this

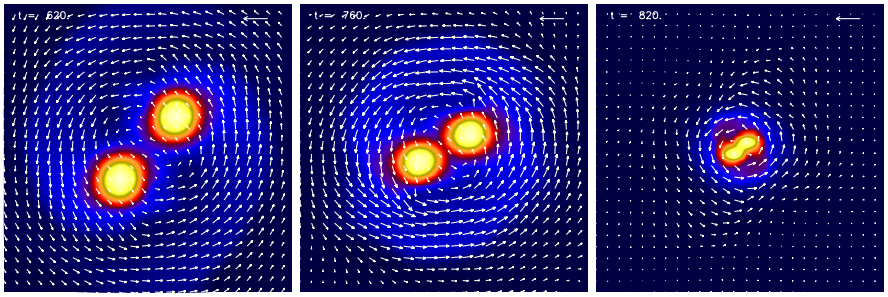

FIG. 11 (color online). Snapshots at select times viewed down the z axis of the orbiting stars and their subsequent collapse to a black hole. These snapshots zoom in on the central region of the grid and show only a twentieth of the $z = 0$ slice of the computational domain. The stars orbit counterclockwise 7 times before merging and collapsing to a black hole. The arrows indicate the fluid velocity. The reference vector in the upper right-hand corner of each panel has a magnitude of 0.5. The color scheme indicates the rest mass density. The plots show the simulation at times 620, 760, and 820 as indicated in the upper left corner of each image. See Fig. 10 for a plot of the lapse at the origin as a function of time for this system.

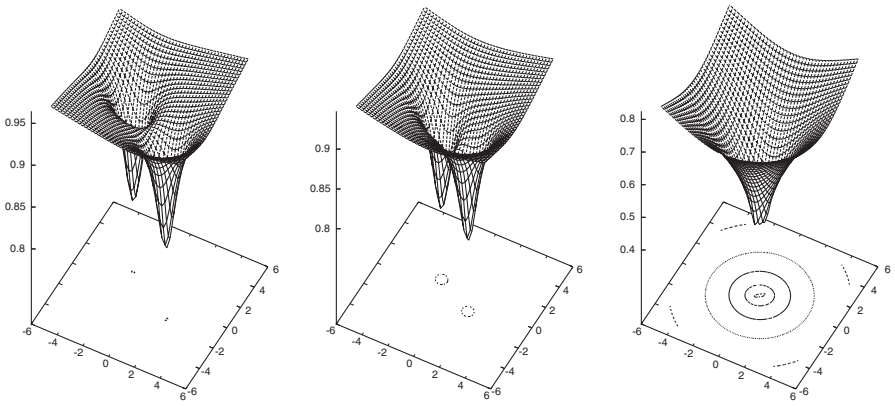

FIG. 12. Snapshots of the lapse on the $z = 0$ plane at times 400, 600, and 820 for the system presented in Fig. 11. The contours shown correspond to $\alpha = 0.8, 0.7, 0.6, 0.5, 0.4$, from the outermost to the innermost one. At times prior to merger, only the first contour value exists. After merger, the lapse collapses, indicating the formation of a black hole. Notice the essentially circular shape of all the contours except for the innermost one at the latest time. The lapse at the origin as a function of time is shown in Fig. 10.

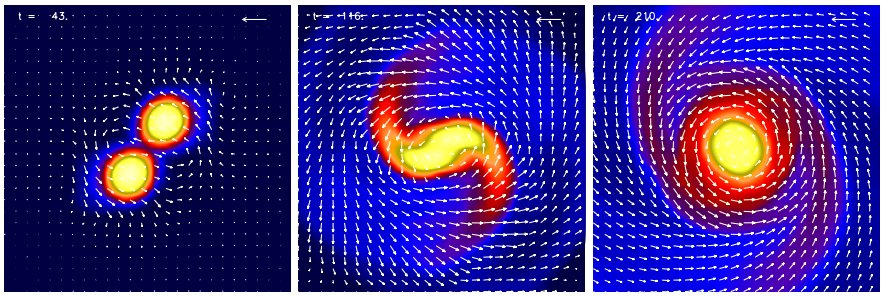

FIG. 13 (color online). Snapshots at select times viewed down the z axis of the orbiting stars and their subsequent merger into a differentially rotating star. These snapshots zoom in on the central region of the grid and show only a twentieth of the $z = 0$ slice of the computational domain. The stars orbit counterclockwise a couple of times before merging. The arrows indicate the fluid velocity. The reference vector in the upper right-hand corner of each panel has a magnitude of 0.5. The color scheme indicates the rest mass density. The plots show the simulation at times 43, 116, and 210 as indicated in the upper left corner of each image. See Fig. 10 for a plot of the lapse at the origin as a function of time for this system.

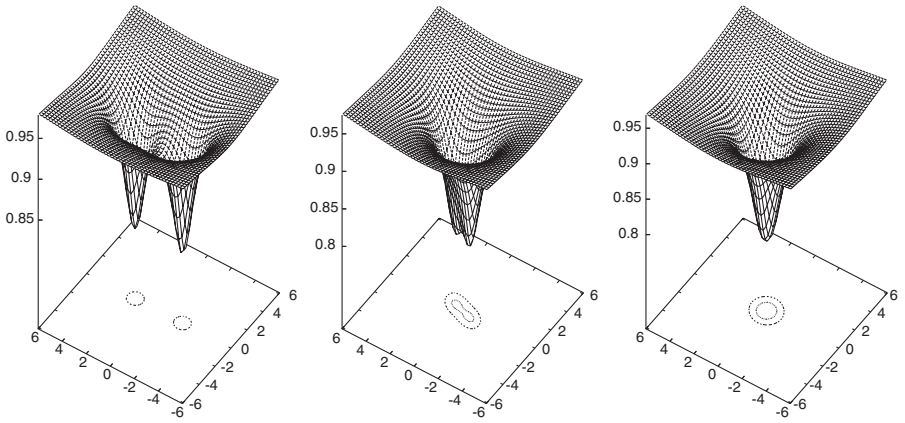

FIG. 14. Snapshots of the lapse on the $z = 0$ plane at times 0, 100, and 200 for the system presented in Fig. 13. The contours shown correspond to $\alpha = 0.9, 0.85$ from the outermost to the innermost one. At early times, the contour for the lowest value is not present. After merger, though the lapse evolves to a slightly lower value, it remains bounded above $\simeq 0.75$. Notice the essentially circular shape of all the contours at the latest time. The lapse at the origin as a function of time is shown in Fig. 10.

evolution agrees with the results presented for the fully relativistic simulation labeled "E-1" in [12], and even with the results from the post-Newtonian SPH simulation labeled "F1" in [62]; compare, for example, our Fig. 15 with Fig. 11 in [12] and Fig. 3 in [62]. These two earlier simulations also followed the merger of equal-mass, initially irrotational neutron stars having a $\Gamma = 2$ equation of state. However, the barlike structure survives noticeably longer in our simulation than in the evolution presented in [62], and in our simulation the radiation signature appears to carry more detail about the postmerger dynamics than in either of these earlier evolutions. Specifically, the structure discernible in Fig. 15 between the times 180 and 240 reflects the fact that, as viewed from the corotating frame of the bar, the bar itself is experiencing nontrivial oscillations.

The neutron star that forms from this merger is strongly differentially rotating. In an effort to quantify this, in the latter stages of the evolution we fit the internal motions of the star to a rotation law of the form

$$\Omega(r) = \frac{\Omega_c}{1 + Ar^2 \sin(\theta)^2} \tag{31}$$

which has proven to be useful in numerous other investigations (see, for instance, [12,63,64]). Figure 16 shows the time-dependent behavior of the fitted parameters Ω_c and A. We note, in particular, that the ratio of the central and near-surface value of Ω at the equator is $\Omega_c/\Omega_{\rm eq} \approx 0.34$.

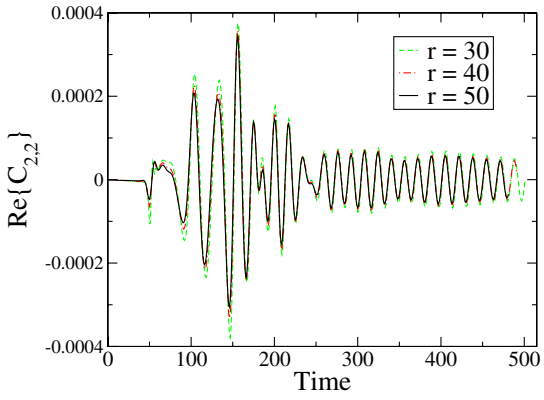

FIG. 15 (color online). The merger waveform for the collision resulting in a single compact star extracted at three different stellar radii: 30, 40, and 50. The domain of the simulation is ± 152 stellar radii. After the merger a transient behavior is observed. In particular, the features at $t \simeq 180$, 240 result from marked oscillations in the produced barlike configuration (as seen in the corotating frame). Afterwards the gravitational waves due to the spinning bar exhibit a clear frequency at $\simeq 12.8$ kHz.

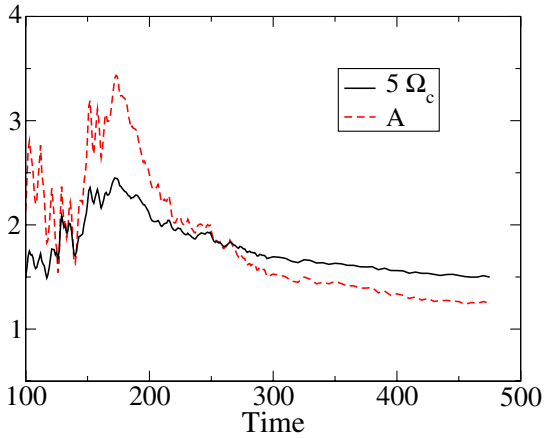

FIG. 16 (color online). The fitted values of Ω_c and A as determined from the fluid's tangential velocity. The merger takes place at about $t \simeq 140$ after which the angular velocity rises during a transient stage and then slowly decreases.

VI. CONCLUSION

Neutron stars will be important sources of gravitational waves for the next generation of gravitational wave detectors. While waveforms from neutron star binaries are weaker than those produced by binary black holes due to the allowed neutron star masses, their signals are expected to be richer, as the gravitational waves will also carry information about the matter. Indeed, gravitational waves are expected to become an important probe of neutron star physics, addressing questions such as the equation of state for nuclear matter and the nature of progenitors for short, hard gamma-ray bursts.

We have constructed a code that solves the combined Einstein and fluid equations in three spatial dimensions, with no symmetry assumptions, and we use HAD for distributed AMR. AMR is an essential element of our method, as it allows us to place the outer boundaries far from the binary, while the shadow hierarchy allows us to refine each star individually without *a priori* assumptions about their motion. We have carefully verified our numerical results by performing runs at different resolutions, using grids with different physical outer boundaries, extracting Ψ_4 at different radii, and varying the floor applied to the fluid densities. Moreover, we studied the radial pulsation frequencies for a $\Gamma = 2$ polytropic TOV star, finding excellent agreement between our results and the expected perturbative values. The successful conclusion of these tests gives us confidence in the physical results obtained from our code.

As a first application of this code in a demanding scenario, we present a detailed study of two binary neutron star mergers, one resulting in a final black hole and the other a final neutron star. In both cases we examine the gravitational wave emission by extracting the $\ell = 2$, $m = 2$ mode of $r\Psi_4$. Ψ_4 is extracted sufficiently far from the binary within the wave zone, and extraction is done at three different radii. In the first case, Ψ_4 is extracted up until the lapse collapses, and in the second case the wave signal is extracted until a final differentially rotating star is reached. A comparison to a post-Newtonian analysis allows us to better understand the gravitational wave signals and the orbital kinematics, such as orbital trajectories, frequencies, and eccentricities. For example, the initial data describe an eccentric orbit. The effect of the eccentricity can be observed in the alternating pattern of larger and smaller extrema in Ψ_4, as well as a modulation in the observed wavelength. Both features are expected from a post-Newtonian analysis of an eccentric orbit. The orbits circularize through gravitational wave emission, and the solution around the time of collapse is largely spherically symmetric. In the second case, the neutron star merger results in a large, strongly differentially rotating star. The observed maximum density after the merger does not lie at the origin but oscillates, in the corotating frame, in a bar-like fashion in between $\simeq 0.2R_{\rm final}$ and $\simeq 0.4R_{\rm final}$ (with $R_{\rm final}$ the equatorial radius of the merged object).

The work presented here raises additional questions that we will pursue in a continuing research program. For example, we will continue to study the ringdown of the final black hole formed in the first merger. Studies of the second case, in which a differentially rotating star is formed, continue in an effort to determine whether this star eventually collapses to form a black hole. We will also examine a broader class of initial data, including quasicircular and unequal mass binaries. As mentioned previously, we also are investigating the effect of magnetic fields on the massive compact object formed in a merger and its possible subsequent collapse. These results will be published in subsequent papers.

ACKNOWLEDGMENTS

We would like to thank J. Frank, J. Pullin, I. Olabarrieta, and O. Reula for stimulating discussions. This work was supported by the National Science Foundation under Grant No. PHY-0326311, No. PHY-0554793, No. AST-0407070, and No. AST-0708551 to Louisiana State University, No. PHY-0326378 and No. PHY-0502218 to Brigham Young University, and No. PHY-0325224 to Long Island University. This research was also supported in part by the National Science Foundation through TeraGrid resources provided by SDSC under Grant No. PHY-040027. In addition to TeraGrid resources, we have employed clusters belonging to the Louisiana Optical Network Initiative (LONI), and clusters at LSU (mike) and BYU (marylou4).

APPENDIX

It is customary in general relativity to adopt geometrized units $G = c = 1$, such that all quantities, including mass (M) and time (T), have units of length (L). Vacuum solutions are invariant under changes in this fundamental length scale L. A quantity X that scales as $L^l M^m T^t$ can be converted into geometrized units by multiplying with the factor $c^t(G/c^2)^m$. After the conversion to geometrized units, X scales as L^{l+m+t}. Most equations of state break this intrinsic scale invariance, and the fundamental length scale must be fixed by additional choices. Once the new scale is chosen, transformations between geometrized and physical units can be easily made. In the following, we summarize the basic procedure detailed in [55] to account for the proper scaling of quantities.

The polytropic EOS (24) is specified by the constants $\{\kappa, \Gamma\}$, and the quantities obtained when using a particular set $\{\kappa_1, \Gamma_1\}$ can be scaled to those obtained using a second set $\{\kappa_2, \Gamma_2\}$ by the factor

$$\frac{L_1}{L_2} = \frac{{\kappa_1}^{1/2(\Gamma_2-1)}}{{\kappa_2}^{1/2(\Gamma_2-1)}}. \tag{A1}$$

There are two common approaches in the literature to set

this additional length scale. The first one is obtained by fixing a constant physical quantity, e.g., the solar mass $M_\odot = 1$, and from it deducing the appropriate conversion factors. That is, if a quantity $\hat{X}$ has dimensions of $L^l M^m T^t$, its dimensionless counterpart, X, is obtained from the following equation:

$$\hat{X} = \left(\frac{GM_\odot}{c^2}\right)^{l+t} \frac{M_\odot^m}{c^t} X. \tag{A2}$$

There is still the freedom to choose κ, and all dimensions are scaled with this parameter. Usually the choice $\kappa = 100$ is preferred because it leads to physical units which are close to the current observations. For instance, TOV stars constructed with these parameters have a maximum stable mass of $\hat{M}_{\max} = 1.64 M_\odot$ with a radius of $\hat{R}_{\max} = 14.11$ km.

The second method for choosing the length scale is explained in detail in [55], and is more involved. It is based on fixing the maximum stable mass for the family of solutions (with given $\{\kappa = 1, \Gamma\}$) to a physically motivated value. Thus, a quantity $\hat{X}$ with dimensions $L^l M^m T^t$ is obtained by using the relation

$$\hat{X} = \hat{\kappa}^x c^y G^z X, \tag{A3}$$

where

$$x = \frac{l + m + t}{2(\Gamma - 1)}, \qquad y = \frac{(\Gamma - 2)l + (3\Gamma - 4)m - t}{\Gamma - 1}, \qquad z = -\frac{l + 3m + t}{2}. \tag{A4}$$

In this method $\hat{\kappa}$ has dimensions. We now identify the maximum stable mass for the given polytrope to some physical maximum mass. For a neutron star, the observed maximum mass is $\hat{M}_{\max} = 1.4 M_\odot$.

Although this second method for fixing the fundamental length scale generally leads to different results from the first, it can be checked that for $\Gamma = 2$ both methods (the first one with $\kappa = 100$, while the second one always has $\kappa = 1$) provide the same scaling factors when the physical maximum stable mass is set to $\hat{M} = 1.64 M_\odot$. Since the dimensionless maximum stable mass is $M = 0.164$, Eq. (A3) can be solved for $\hat{\kappa}$ with $\{l = 0, m = 1, t = 0\}$, giving $\hat{\kappa} = 1.456 \times 10^5$ cm^5/(g s^2). With this value, (A3) can again be used to recover the dimensions of any quantity.

[1] G. Harry, J. Houser, and K. Strain, Phys. Rev. D **65**, 082001 (2002).
[2] I. Mandel, D. A. Brown, J. R. Gair, and M. C. Miller, arXiv:0705.0285.
[3] F. Pretorius, Phys. Rev. Lett. **95**, 121101 (2005).
[4] M. Campanelli, C. Lousto, P. Marronetti, and Y. Zlochower, Phys. Rev. Lett. **96**, 111101 (2006).
[5] J. Baker, J. Centrella, D. Choi, M. Koppitz, and J. van Meter, Phys. Rev. Lett. **96**, 111102 (2006).
[6] P. Diener, F. Herrmann, D. Pollney, E. Schnetter, E. Seidel, R. Takahashi, J. Thornburg, and J. Ventrella, Phys. Rev. Lett. **96**, 121101 (2006).
[7] J. Gonzalez, U. Sperhake, B. Brugmann, M. Hannam, and S. Husa, Phys. Rev. Lett. **98**, 091101 (2007).
[8] B. Szilagyi, D. Pollney, L. Rezzolla, J. Thornburg, and J. Winicour, Classical Quantum Gravity **24**, S275 (2007).
[9] A. Bounanno, G. B. Cook, and F. Pretorius, Phys. Rev. D **75**, 124018 (2007).
[10] Y. Pan, A. Bounanno, J. Baker, J. Centrella, B. Kellly, S. McWilliams, F. Pretorius, and J. van Meter, arXiv:0704.1964 [Phys. Rev. D (to be published)].
[11] T. Baumgarte *et al.*, arXiv:gr-qc/0612100.
[12] M. Shibata and K. Uryu, Prog. Theor. Phys. **107**, 265 (2002).
[13] M. D. Duez, P. Marronetti, S. L. Shapiro, and T. W. Baumgarte, Phys. Rev. D **67**, 024004 (2003).
[14] M. Shibata, K. Taniguchi, and K. Uryu, Phys. Rev. D **68**, 084020 (2003).
[15] M. A. Miller, P. Gressman, and W.-M. Suen, Phys. Rev. D **69**, 064026 (2004).
[16] P. Marronetti, M. D. Duez, S. L. Shapiro, and T. W. Baumgarte, Phys. Rev. Lett. **92**, 141101 (2004).
[17] K.-J. Jin and W.-M. Suen, Phys. Rev. Lett. **98**, 131101 (2007).
[18] M. Shibata, K. Taniguchi, and K. Uryu, Phys. Rev. D **71**, 084021 (2005).
[19] M. Shibata and K. Uryu, Phys. Rev. D **74**, 121503 (2006).
[20] M. Shibata and K. Uryu, Classical Quantum Gravity **24**, S125 (2007).
[21] F. Löffler, L. Rezzolla, and M. Ansorg, Phys. Rev. D **74**, 104018 (2006).
[22] C. Palenzuela, I. Olabarrieta, L. Lehner, and S. Liebling, Phys. Rev. D **75**, 064005 (2007).
[23] C. Palenzuela, L. Lehner, and S. Liebling, arXiv:0706.2435.
[24] D. Neilsen, E. W. Hirschmann, and R. S. Millward, Classical Quantum Gravity **23**, S505 (2006).
[25] M. Anderson, E. Hirschmann, S. L. Liebling, and D. Neilsen, Classical Quantum Gravity **23**, 6503 (2006).
[26] L. Lehner, S. L. Liebling, and O. Reula, Classical Quantum Gravity **23**, S421 (2006).
[27] L. Lindblom, M. A. Scheel, L. E. Kidder, R. Owen, and O. Rinne, Classical Quantum Gravity **23**, S447 (2006).
[28] C. Gundlach, J. Garcia, G. Calabrese, and I. Hinder, Classical Quantum Gravity **22**, 3767 (2005).
[29] J. M. Marti and E. Müller, Living Rev. Relativity **2**, 3

(1999).
[30] J. A. Font, Living Rev. Relativity **3**, 2 (2000).
[31] S. K. Godunov, Mathematics of the USSR Sbornik **47**, 271 (1959).
[32] M. Anderson, E. W. Hirschmann, L. Lehner, S. L. Liebling, P. Motl, N. David, C. Palenzuela, and J. E. Tohline (unpublished).
[33] O. A. Reula, Living Rev. Relativity **1**, 3 (1998).
[34] http://www.had.liu.edu/.
[35] S. L. Liebling, Phys. Rev. D **66**, 041703 (2002).
[36] R. Hornung, S. Kohn, N. Elliott, S. Smith, A. Wissink, B. Gunney, and D. Hysom, http://www.llnl.gov /CASC/ SAMRAI/.
[37] L. B. N. L. Applied Numerical Algorithms Group, http:// seesar.lbl.gov/anag/chombo/.
[38] P. MacNeice, K. Olson, C. Mobarry, R. deFainchtein, and C. Packer, Comput. Phys. Commun. **126**, 330 (2000).
[39] R. Deiterding, http://amroc.sourceforge.net/.
[40] M. Lijewki, V. Beckner, and C. Rendleman, http://seesar. lbl.gov/ccse/Software/index.html.
[41] M. J. Berger and J. Oliger, J. Comput. Phys. **53**, 484 (1984).
[42] M. Berger and I. Rigoutsos, IEEE Transactions on Systems Science and Cybernetics **21**, 1278 (1991).
[43] C. Rendleman, V. Beckner, M. Lijewski, W. Crutchfield, and J. Bell, Comput. Visual Sci **3**, 147 (2000).
[44] K. Sebastian and C.-W. Shu, J. Sci. Comput. **19**, 405 (2003).
[45] C.-W. Shu and S. Osher, J. Comput. Phys. **83**, 32 (1989).
[46] B. Gustaffson, H.-O. Kreiss, and J. Oliger, *Time Dependent Problems and Difference Methods* (John Wiley & Sons, New York, 1995).
[47] G. Calabrese, L. Lehner, O. Reula, O. Sarbach, and M. Tiglio, Classical Quantum Gravity **21**, 5735 (2004).
[48] O. Rinne, L. Lindblom, and M. A. Scheel, Classical Quantum Gravity **24**, 4053 (2007).
[49] X.-D. Liu and S. Osher, J. Comput. Phys. **142**, 304 (1998).
[50] L. Del Zanna and N. Bucciantini, Astron. Astrophys. **390**, 1177 (2002).
[51] A. Harten, P. D. Lax, and B. van Leer, SIAM Rev. **25**, 35 (1983).
[52] P. Colella and P. R. Woodward, J. Comput. Phys. **54**, 174 (1984).
[53] N. Stergioulas and S. Morsink, http://www.gravity.phys. uwm.edu/rns/.
[54] J. A. Font, T. Goodale, S. Iyer, M. Miller, L. Rezzolla, E. Seidel, N. Stergioulas, W.-M. Suen, and M. Tobias, Phys. Rev. D **65**, 084024 (2002).
[55] S. Noble, Ph.D. thesis, University of Texas at Austin, 2003 (Appendix 1).
[56] R. A. Matzner, M. F. Huq, and D. Shoemaker, Phys. Rev. D **59**, 024015 (1998).
[57] L. Lehner and O. M. Moreschi, arXiv:0706.1319.
[58] M. Anderson *et al.* (unpublished).
[59] T. Mora and C. Will, Phys. Rev. D **66**, 101501 (2002).
[60] M. Alcubierre, Classical Quantum Gravity **20**, 607 (2003).
[61] M. Anderson, E. W. Hirschmann, L. Lehner, S. L. Liebling, P. Motl, D. Neilsen, C. Palenzuela, and J. E. Tohline (unpublished).
[62] J. A. Faber and F. A. Rasio, Phys. Rev. D **65**, 084042 (2002).
[63] I. Hachisu, Astrophys. J. **61**, 479 (1986).
[64] N. D. Lyford, T. W. Baumgarte, and S. L. Shapiro, Astrophys. J. **583**, 410 (2003).